Dynamic Activation of Single Atom Catalysts by Reaction Intermediates: Conversion of Formic Acid on $Rh/Fe_3O_4(001)$

Christopher J. Lee[1,†], Marcus A. Sharp[1,2,†], Benjamin A. Jackson,[1,†] Mausumi Mahapatra[1], Simone Raugei,[1] Líney Árnadóttir,[1,3] Mal-Soon Lee,[1*] Bruce D. Kay[1], and Zdenek Dohnálek[1,2*]

[1] Physical and Computational Sciences Directorate and Institute for Integrated Catalysis, Pacific Northwest National Laboratory; Richland, Washington 99354, USA.

[2] Voiland School of Chemical Engineering and Bioengineering, Washington State University; Pullman, Washington 99163, USA.

[3] School of Chemical, Biological, and Environmental Engineering, Oregon State University; Corvallis, Oregon 97331, USA.

Keywords: Catalyst dynamics, $Fe_3O_4(001)$, Rhodium, single atom catalysis, formic acid.

Abstract: The stability and activity of supported single-atom catalysts (SACs) represent critical yet opposing factors limiting our ability to explore and exploit their unique properties. This study demonstrates the operation of a switchable catalyst that is activated in the presence of surface intermediates and reverts to a stable but inactive form when the reaction is completed. We employ atomically defined $Rh/Fe_3O_4(001)$ catalysts to demonstrate how structurally stable Rh, bound in surface octahedral Fe sites, gets destabilized to form highly active Rh adatoms and small clusters. Conversion of formic acid, leading initially to surface formate and hydroxyl species, is employed as a model reaction to probe the dynamics of such processes. We find that surface hydroxyl recombination to water through the Mars-van Krevelen mechanism reduces Rh coordination, triggering its conversion to active Rh adatoms. Since such lattice oxygen exchange is observed in many acid-base and redox chemistries, the process can be broadly applicable to controlling the activation of the range of SACs.

1. INTRODUCTION

Understanding the dynamic changes occurring at catalytic active sites under reaction conditions is a significant challenge that hampers the design of future catalysts. The ultimate objective of creating highly active sites is tempered by their stability.[1-4] The key solution to this problem lies in our ability to dynamically activate and partially destabilize the catalytic site structure by introducing reactants, intermediates, and co-adsorbates.[5-7] In this context, supported single-atom catalysts (SACs) have emerged as a frontier in fundamental catalytic research. Despite their general instability, SACs possess inherent potential for novel reaction pathways and exhibit high selectivity compared to their nanoparticulate counterparts.[8-16] These distinctive catalytic properties arise from their ionic nature, predominantly homotopic environment, and undercoordinated character.[2, 17-20] Furthermore, when studied in liquid environments, SACs are a unique parallel to homogeneous catalysts.[16, 21-22] However, identifying their binding configuration and environment during the reaction process poses immense challenges, and as such, the active sites remain poorly characterized and likely different from their resting state.[1, 23-24]

In this regard, model systems that can be characterized at the atomic level can yield important details about such dynamic processes under reaction conditions. In recent years, single metal atoms supported on $Fe_3O_4(001)$ emerged as an ideal platform where single metal atoms are relatively strongly bound as adatoms to two lattice oxygens.[25-26] The vacuum stability of many single metal atoms has been well- characterized yielding a wealth of information about their behavior. In several cases (Pd, Pt, Ag), the destabilization of single atoms by strongly bound adsorbates such as CO and methanol has been shown,[6, 27-28] while stabilization of Rh and Ir single atoms by CO has also been demonstrated.[29-30] Further, Rh adatoms (Rh_{ad}) and Rh nanoparticles (Rh_{met}) bare active toward CO oxidation and CO_2 reduction reactions.[30-31] Rh supported on $Fe_3O_4(001)$ studied here was selected due to its ability to form stable mixed oxide surfaces from the Rh adatoms.[10, 30-31] It has been demonstrated that single Rh_{ad}'s will, upon annealing between 500 and 700 K, substitute into the surface Fe octahedral sites, forming Rh octahedral (Rh_{oct}) sites and yielding thermally stable mixed $Rh_{oct}/Fe_3O_4(001)$ surfaces.[30-31]

This binding configuration has also been shown to be the most stable on high surface area catalysts.[32-33] High-temperature annealing (900 K) leads to Rh segregation and the formation of large nanoparticles.[31] Similarly, annealing Rh/α-$Fe_2O_3(1\bar{1}02)$ systems results in the incorporation of Rh into the oxide lattice, whereas mild oxidizing conditions can even promote the dissolution of larger Rh clusters into the surface,[34] while Rh_{ad} sites on the α-$Fe_2O_3(1\bar{1}02)$ surface are both

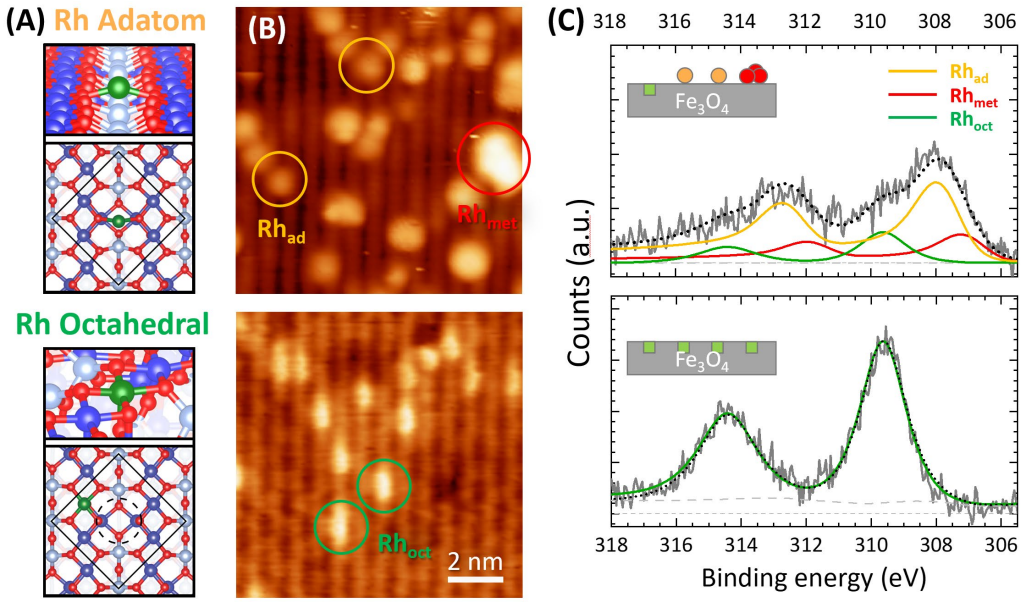

Figure. 1. STM and XPS characterization of Rh_{ad} and Rh_{oct} sites. (A) Schematic models showing side and top view of reconstructed $Fe_3O_4(001)$ unit cell with Rh_{ad} (top) and Rh_{oct} (bottom) atoms indicated in cyan. Fe_{oct} is shown in blue, Fe_{tet} grey, Rh_{ad} cyan, and O red. The yellow square shows the unit cell (u.c.) of the surface reconstruction and the black circle denotes the bulk-like open (BLO) site. (B) STM images (V_s = 1.4-1.7 V, I = 0.2 nA) acquired after the deposition of 0.2 Rh/u.c. at 293 K (top) and after post-annealing at 700 K (bottom). Several Rh_{ad}, Rh_{oct}, and Rh_{met} species are highlighted by yellow-orange, green, and red circles, respectively. (C) Rh 3d XPS spectra of Rh adatoms after the deposition of 0.17 Rh/u.c. at 250 K (Rh_{ad}, top panel) bound on $Fe_3O_4(001)$ and post-annealing at 700 K producing Rh that is octahedrally-coordinated (Rh_{oct}, bottom panel) in the $Fe_3O_4(001)$. The acquired spectra (dark gray) are fitted (black dots) using Rh_{oct} (green), Rh_{ad} (yellow-orange), and Rh_{met} (red) components. The background from bare $Fe_3O_4(001)$ is shown in light gray. The fitting methods and parameters are outlined in Ref. 31.

stabilized and dispersed in low-pressure water environments.[34]

We selected formic acid as a probe molecule to test the stability, dynamic interconversion, and activity of distinct Rh sites on $Fe_3O_4(001)$. The probing of catalyst sites with formate can yield important information regarding the acid-base properties and redox activity of the surface sites. For instance, in CO_2 reduction, formate is often proposed as an intermediate species toward the formation of methane, methanol, and CO.[8, 35-37] In many oxygenate reactions, where carboxylate intermediates are common, the reaction pathways to different products depend on the surface acid-base or redox properties.[38-45] The reaction of formic acid on metal oxides generally occurs via dehydrogenation (CO_2, H_2CO, and H_2 products) or dehydration reaction (CO and H_2O) with more reducible oxide surfaces/catalysts shifting the selectivity toward dehydrogenation, illustrating the surface sites are more redox active. Formic acid deprotonates readily on $Fe_3O_4(001)$ at 300 K, leaving behind an acidic hydrogen bound in the form of a surface hydroxyl species and a bidentate formate species bound to two neighboring Fe octahedral sites.[46] These can yield H_2 and/or H_2O, with H_2O formation providing a mechanistic path to incorporate surface oxygen in the reaction products via the Mars-van Krevelen mechanism.[43, 45] As we show here, this process is critical for the dynamic creation of the catalytically active Rh sites.

This study demonstrates how thermally stable octahedral Rh atoms incorporated in the $Fe_3O_4(001)$ surface are dynamically released and activated toward formic acid conversion. We show that during the reaction, octahedral Rh sites are converted to Rh adatoms and small clusters that act as active sites for formate reduction to CO_2. While formic acid on $Fe_3O_4(001)$ dehydrates and yields primarily CO, extremely small coverages of Rh adatoms separated by tens of nanometers (~0.01 Rh/u.c., unit cell) shift the surface kinetics towards the CO_2 selective dehydrogenation pathway. Additional hydrogenation studies of Rh_{oct}-$Fe_3O_4(001)$ surfaces reveal that water formation from surface hydroxyl species via Mars-van Krevelen mechanism[47] is responsible for the destabilization of Rh_{oct}, likely due to reduced surface oxygen coordination. The conclusions from the experimental studies are further corroborated by Density Functiona Theory calculations.

2. RESULTS

2.1 Preparation and characterization of model Rh/$Fe_3O_4(001)$ catalysts. Previous studies have established two distinct forms of single-atom Rh catalysts on $Fe_3O_4(001)$: Rh adatoms (Rh_{ad}), which bond to two undercoordinated oxygen atoms on the surface, and in-surface octahedral Rh atoms (Rh_{oct}) that have replaced one of the octahedral Fe (Fe_{oct}).[30-31] Figure 1 provides spectroscopic and imaging signatures, along with a schematic representation of these single atom sites.

In Figure 1A, the top schematic view illustrates the geometric configuration of the Rh_{ad} (cyan) bound to the reconstructed $Fe_3O_4(001)$. Each Rh_{ad} is bonded to two surface oxygen atoms (red) spanning adjacent Fe_{oct} rows (blue), centered above the bulk-like open (BLO, black circle) site—i.e., a site without

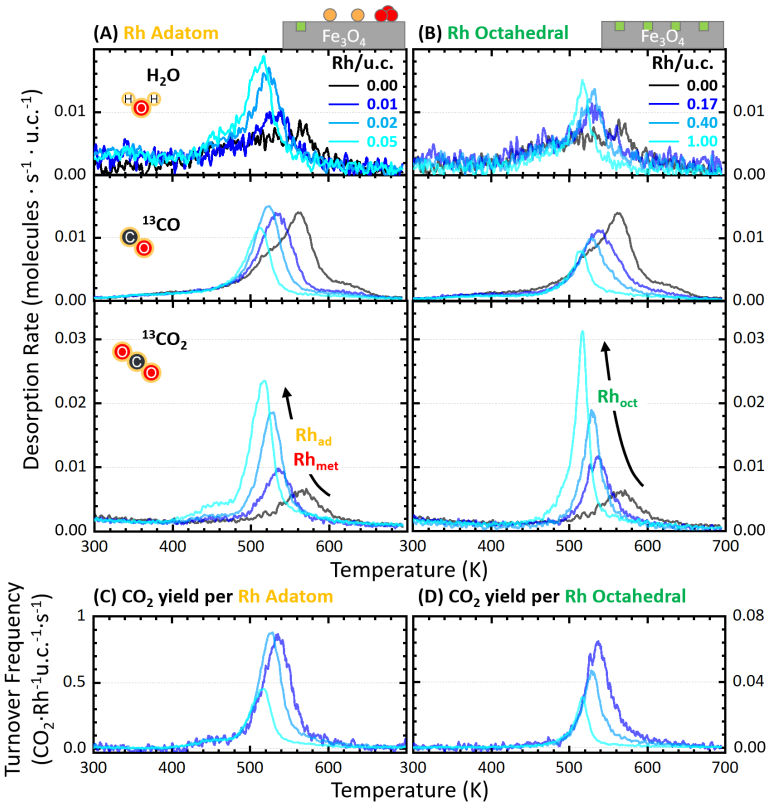

Figure. 2. TPRS of products (H_2O - top, ^{13}CO - middle, $^{13}CO_2$ - bottom) observed from the saturation dose of $H^{13}COOH$ on $Rh/Fe_3O_4(001)$ model catalysts. (A) $Rh/Fe_3O_4(001)$ catalysts dominated by Rh_{ad} and Rh_{met} active sites prepared by Rh deposition (0-0.05 Rh/u.c.) at 250 K. (B) $Rh/Fe_3O_4(001)$ catalysts dominated by Rh_{oct} sites prepared by Rh deposition at 250 K and annealing to 700 K (0.17-0.40 Rh/u.c.) or deposition at 700 K (1.0 Rh/u.c.). (C and D) $^{13}CO_2$ turnover frequencies in $CO_2 \cdot Rh^{-1}u.c.^{-1}s^{-1}$ along the TPRS ramp from (A) and (B), respectively.

tetrahedral Fe (Fe_{tet}, gray) underneath. The bottom schematic view shows the structure of the Rh_{oct} (cyan) formed by displacing one of the Fe_{oct} atoms from Rh_{ad} upon annealing at 500-700 K.

The scanning tunneling microscopy (STM) images in Figure 1B depict the appearance of Rh_{ad} and Rh_{oct}. The top image predominantly shows bright Rh_{ad} species (several highlighted by yellow-orange circles) situated between the bright Fe_{oct} rows. Additionally, the image reveals a few aggregates of several atoms in size (one highlighted by the red circle, Rh_{met}). The bottom image displays Rh_{oct} sites prepared by annealing the as-prepared Rh_{ad} surface (top) at 700 K.

Figure 1C displays the Rh 3d X-ray photoelectron spectroscopy (XPS) spectra obtained after preparing 0.17/u.c. Rh_{ad}- and Rh_{oct}-dominated surfaces. Decomposition of distinct Rh signatures[30-31] shows that, as an ensemble average, the deposition of Rh at 250 K (top) results in a surface dominated by isolated Rh_{ad}'s, and a small proportion of Rh_{oct}. To avoid the formation of small Rh clusters (Rh_{met}) (one seen for 0.17 Rh/u.c. in Figure 1B top), using low Rh coverages (<0.1 Rh/u.c.) is essential. Annealing Rh_{ad} covered-surfaces (<0.5 Rh/u.c.) at 700 K leads to completely incorporating all Rh species into the oxide surface layer as Rh_{oct}, *i.e.*, the absence of the observed Rh_{ad} or Rh_{met} species, Figure 1C bottom.

The existence of these two distinct single Rh atom configurations offers a unique opportunity to compare and contrast their catalytic chemistry. For this purpose, formic acid is selected as the prototypical molecule, enabling the exploration of acid-base and redox chemistry reaction pathways leading to the formation of CO and CO_2, respectively.[38-45] Furthermore, the initial deprotonation of formic acid yields formate and surface hydroxyls, which play crucial roles as surface species during CO_2 dehydrogenation reactions.[38-45]

2.2 Coverage-dependent product formation on Rh adatom and octahedral sites. Figure 2 illustrates the temperature-programed reaction spectroscopy (TPRS) spectra of the products observed during the reaction of isotopic formic acid ($H^{13}COOH$) adsorbed over $Rh_{ad}/Fe_3O_4(001)$ (Figure 2A) and $Rh_{oct}/Fe_3O_4(001)$ (Figure 2B) model catalysts. Representative XPS spectra obtained from the model 0.05 Rh_{ad}/u.c. before formic acid TPRS and after conversion to Rh_{oct} at 700 K are given in Figure S1. Additionally, XPS from $Rh_{oct}/Fe_3O_4(001)$ with 0.17 and 1.0 Rh/u.c. are shown in Figure 3. Despite the substantial difference in the Rh content, with $Rh_{oct}/Fe_3O_4(001)$ having approximately twenty times more Rh compared to $Rh_{ad}/Fe_3O_4(001)$, there are striking similarities in the behavior of these two systems as the Rh coverage increases (from dark to light blue).

We now focus on a more detailed description of the evolution of the product distribution. The TPRS spectra for formic acid conversion on $Fe_3O_4(001)$ are displayed in black for reference. Within the temperature range of 450-600 K, water is the

sole hydrogen-containing product observed. Additionally, CO and CO_2 are the only carbon-containing products, with CO being the predominant species (~75%).

Upon the addition of a small amount of Rh_{ad} (0.01-0.05 Rh/u.c.) at 250 K, the distribution of carbon-containing products shifts from being CO-dominated (Figure 2A, middle) to CO_2-dominated (Figure 2A, bottom). Further, water, which desorbs as a broad peak from ~420 to 600 K on the $Fe_3O_4(001)$, develops a sharper desorption feature (Figure 2A, top) indicating HCOOH conversion over a narrower temperature range. The peak position for H_2O, CO, and CO_2 shifts to lower temperatures, with CO_2 shifting from approximately 570 K for bare Fe_3O_4 (black traces) to 520 K for 0.05 Rh_{ad}/u.c. This shift indicates that the Rh_{ad} sites become the preferential sites for formate conversion, with the preferential reaction pathway shifting from dehydration to dehydrogenation. It also demonstrates the enhanced redox activity of the Rh adatom site versus the bare oxide. The small shoulder in the CO_2 product is likely due to the reaction of formic acid on sparse Rh clusters, as evidenced by TPRS on a much higher coverage of Rh (1.0/u.c.) deposited at 250 K (Figure S2). In our previous work, we determined that these higher coverages are dominated by Rh clusters.[31] Thus, we can conclude the CO_2 desorption >480 K is due to Rh adatoms and not clusters. Some small clusters likely form through the course of the TPRS despite not being present initially in XPS, Figure S1, and are a result of either adsorbate-induced or thermal destabilization of the adatoms as observed previously.[6,12, 30-31] Assuming isolated Rh_{ad}, the average spacing between the Rh_{ad} along the rows is approximately 8.4 nm for 0.01 Rh/u.c. and 4 nm for 0.05 Rh/u.c. If all the reaction products form on Rh_{ad} active sites, we can deduce that at the lowest Rh_{ad} concentration of 0.01 Rh/u.c., each site turns over an average of approximately 200 formate species during the TPRS ramp. The formation of water follows a similar trend. Also, the water peak shifts to lower temperatures, indicating that its formation is not the rate-limiting step and readily occurs after C-H bond cleavage.

The formic acid conversion to CO_2 on $Rh/Fe_3O_4(001)$ catalysts where all the Rh was converted to Rh_{oct} by annealing to 700 K is significantly less efficient than that of Rh_{ad} (see Figure S3). As the amount of Rh_{oct} increases by approximately an order of magnitude (0.17-1.00 Rh/u.c., Figure 2B), analogous evolution to that on Rh_{ad} is observed in TPRS (H_2O (top), CO (middle), and CO_2 (bottom)). The CO_2 dehydrogenation reaction pathway dominates, and the desorption temperature shifts from 570 to 520 K, similar to the Rh_{ad}/Fe_3O_4 system. Based on the relative yields of CO and CO_2, we conclude that the activity of the Rh_{oct}/Fe_3O_4 systems parallels that of the Rh_{ad}/Fe_3O_4 systems, but the concentration of Rh_{oct} has to be increased ~20 times that of Rh_{ad}

This assessment is quantitatively evaluated by comparing the CO_2 turnover frequencies (Figure 2C and 2D) obtained by normalizing CO_2 desorption rates by the amount of deposited Rh from Figures 2A and 2B. For both Rh_{ad} and Rh_{oct} systems, the leading edges of CO_2 TPRS spectra collapse on a common line independent of the Rh coverage. In the case of Rh_{ad}, this overlap demonstrates that the number of active Rh sites increases linearly with Rh coverage (in the low Rh coverage limit explored here) and that Rh_{ad} remains active during the conversion of formate species to CO_2. This overlap further shows that bidentate formate is sufficiently mobile[46] to reach even the sparsely populated Rh_{ad} sites (~10 nm apart). For the lowest Rh_{ad} coverage of 0.01 Rh/u.c., a slight deviation towards lower turnover frequencies is observed, likely indicating an onset of the limitations in the formate mobility. The integral of CO_2 produced per Rh_{ad} site (turnover number) decreases as the Rh_{ad} coverage increases (Figure 2C), demonstrating that the downshift in peak desorption temperatures results from an increase in active site population rather than an increase in the inherent activity of the Rh active sites.

Despite pre-annealing to 700 K, the Rh_{oct}/Fe_3O_4 system demonstrates analogous behavior (Figure 2D), suggesting that in the presence of formate and hydroxyl species, the Rh_{oct} may be converted to Rh_{ad}. This proposition is plausible as our previous work demonstrated that Rh_{ad} is active toward CO oxidation and CO_2 reduction while Rh_{oct} is not, and this has been reproduced in Figure S4.[31]

2.3 Characterization of Rh active sites during the reaction. To test this hypothesis, we analyze the evolution of the Rh 3d XPS spectra along the TPRS ramp on initially pure $Rh_{oct}/Fe_3O_4(001)$ surfaces covered by formate and hydroxyl species. In Figure 3A, we follow the changes in the abundance of different binding motifs of Rh after adsorbing 2.0 HCOOH/u.c. at 80 K on the surface with 1.0 Rh_{oct}/u.c. following annealing at various temperatures to mimic the conditions of our TPRS experiments. The highest possible Rh_{oct} coverage of 1.0 Rh_{oct}/u.c. is selected to maximize the signal-to-noise in the Rh 3d XPS spectra. The $Rh_{oct}/Fe_3O_4(001)$ surface was prepared by depositing Rh at 700 K, and the resulting Rh 3d XPS spectrum is shown at the top of Figure 3A. Subsequent adsorption of formic acid is carried out at 250 K and results in the formation of formate and lattice-oxygen-containing hydroxyls, as demonstrated for HCOOH on bare $Fe_3O_4(001)$.[46]

Annealing of this HCOOH-saturated $Rh_{oct}/Fe_3O_4(001)$ surface to 500 K yields a middle-top spectrum in Figure 3A that is virtually identical to the initial spectrum (Figure 3A, top). Interestingly, upon annealing to 550 K (middle-bottom, Figure 3A), approximately 13% of the Rh_{oct} converts to Rh_{ad} (4.3%) and Rh_{met} (8.7%). Most of the HCOOH is converted to reaction products at this annealing temperature, as shown in Figure 2B. Additionally, in the Fe 2p XPS spectra (Figure S5A), an increase in the Fe^{2+} shoulder (~709 eV) indicates a reduction of the surface due to hydroxyls and water formation[48] that occurs during the conversion of Rh_{oct} to Rh_{met}. Upon further annealing to 700 K, most (98%) of the Rh_{ad} and Rh_{met} species convert back to Rh_{oct} and the Rh 3d spectrum (bottom, Figure 3A) reverts to that of the initial surface (top, Figure 3A). Only a negligible amount (~2%, within the error bar of the fit) of the Rh_{met} intensity remains, suggesting that the process is reversible.

In our previous study, we demonstrated that small Rh clusters (<1.3 nm) can be redispersed and converted to Rh_{oct} whereas

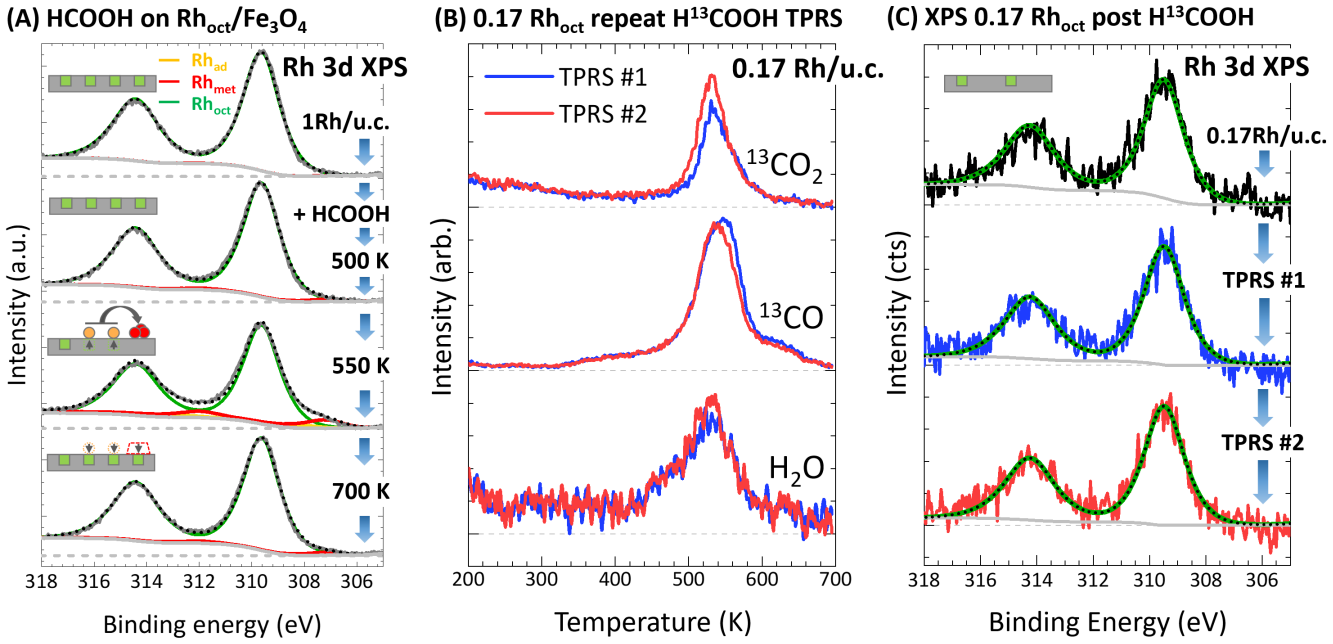

Figure. 3. The evolution of 3d Rh XPS of the initial $Rh_{oct}/Fe_3O_4(001)$ in the presence of formic acid. (A) The initial spectrum from1.0 Rh_{oct}/u.c. (top spectrum) followed by dosing HCOOH at 80 K and flashing to 500 K (middle-top), 550 K (middle-bottom), and 700 K (bottom). (B) Repeat $H^{13}COOH$ TPRS performed on 0.17 Rh_{oct}/u.c. (C) Rh 3d XPS after subsequent exposures of the 0.17 Rh_{oct}/u.c. to $H^{13}COOH$ and after flash to 700 K. The initial spectrum from 0.17 Rh/u.c. (black-top), after 1st exposure (blue-middle), and after 2nd exposure (red-bottom). $Rh_{oct}/Fe_3O_4(001)$ was prepared by depositing Rh at 700 K (1.0 Rh/u.c.) or deposition at 250 K and annealing to 700 K (0.17 Rh/u.c.).

nanoparticles (>2 nm) cannot.[31] Thus, to eliminate the formation of minority Rh_{met} species (Figure 3A), we evaluate the reversible activation of the Rh_{oct} at lower Rh loading of 0.17 Rh_{oct}/u.c. where the average separation between Rh_{oct} is increased by approximately a factor of two. The XPS from 0.17 Rh_{oct}/u.c. before and after two cycles of formic acid exposure, Figure 3B, indicates no measurable change in Rh speciation. The corresponding repeated TPRS experiment carried out on this 0.17 Rh_{oct}/u.c. surface (Figure 3C) further demonstrates the recovery of the original Rh_{oct} surface and, therefore, transient activation to Rh_{ad} in the presence of HCOOH. The slight CO_2 yield increase (~25%) suggests possible additional Rh_{oct} is activated in the 2nd TPRS versus the 1st TPRS.

2.4 The role of hydroxyl species in Rh_{oct} activation. To further decouple the role of formate and hydroxyl species, we adsorbed atomic deuterium on the $Rh_{oct}/Fe_3O_4(001)$ surface, forming surface hydroxyl species without formate. The amount of adsorbed D atoms was calibrated by attenuating ($\sqrt{2}$ x $\sqrt{2}$) LEED spots. As shown previously, hydroxylation leads to the lifting of the ($\sqrt{2}$ x $\sqrt{2}$) reconstruction,[48] and, as such, serves as a good measure of D coverage. Figure 4A displays the evolution of Rh 3d XPS spectra from a pure 0.3 Rh_{oct}/u.c. surface (top spectrum) where ($\sqrt{2}$ x $\sqrt{2}$) was attenuated to 50%, corresponding to a D coverage of ~1/u.c.[48] Exposure to D at 400 K has a negligible effect on the spectrum (middle-top, Figure 4A) even though the Fe 2p shows surface reduction (Figure S5B) due to hydroxyl formation, indicating hydroxyls alone do not destabilize Rh_{oct}. When the surface is exposed to an additional identical dose of D at 500 K, approximately 24% of the Rh_{oct} converts to Rh_{ad} (7%) and Rh_{met} (17%) (middle-bottom, Figure 4A). Subsequently, flashing the sample to 700 K leads to the conversion of Rh_{ad} and Rh_{met} species back to Rh_{oct} (bottom, Figure 4A). Similar to the formic acid adsorption experiment, only a small amount of Rh remains in the form of Rh_{met} (~3%) after the flash. In both cases, the conversion of Rh_{oct} to Rh_{ad} and Rh_{met} is initiated between 500 and 550 K, suggesting the reaction of hydroxyl species and not formate destabilizes Rh_{oct}. The experiment with atomic hydrogen (Figure 4A) demonstrates that surface hydroxyls are responsible for converting Rh_{oct} to Rh_{ad} and Rh_{met} rather than the formate species.

Further evidence for the effect of surface hydroxyls on the surface morphology comes from STM imaging of the $Rh/Fe_3O_4(001)$ surfaces (pre-annealed to 700 K) that have both Rh_{oct} and Rh_{met} sites (Figure 4B). Here, H_2 dissociation on Rh clusters (rather than direct exposure to hydrogen atoms) leads to surface hydroxylation[12, 47] of the initial Rh_{oct} + $Rh_{met}/Fe_3O_4(001)$ surface (top, Figure 4B). The surface hydroxylation significantly increases Rh cluster coverage at 500 K (middle, Figure 4B). This indicates that under hydrogenation conditions where H_2 dissociation is facilitated by Rh_{met}, the Rh_{oct} also becomes destabilized and released from the $Fe_3O_4(001)$ lattice. The proof of surface hydroxylation comes from the images obtained at 700 K, where surface hydroxyls recombine and yield water via Mars-van Krevelen mechanism.[47] The resulting etch pits demonstrate lattice oxygen removal from the surface.

As shown in the top panels of Figure 2, water forms from surface hydroxyls at 500-550 K. This temperature range overlaps exactly with the Rh_{oct} release temperature. As such, these

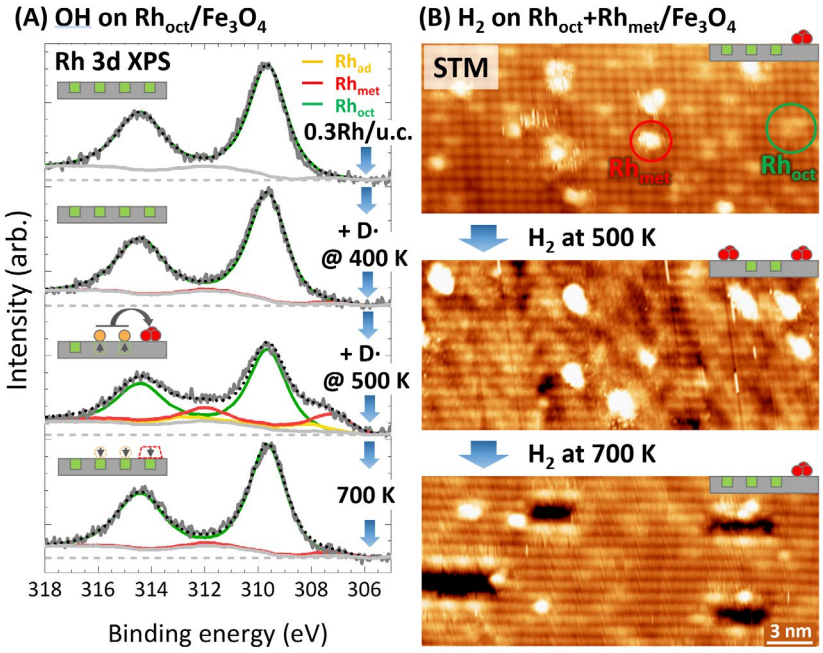

Figure. 4. The evolution of 3d Rh XPS of the initial $Rh_{oct}/Fe_3O_4(001)$ in the presence of hydroxyls or hydrogen. $Rh_{oct}/Fe_3O_4(001)$ was prepared by depositing Rh at 700 K. (A) The initial spectrum from 0.3 Rh/u.c. (top spectrum) followed by deposition of atomic deuterium at 400 K (middle-top), followed by additional deposition of atomic deuterium at 500 K (middle-bottom), and UHV flash to 700 K (bottom). All XPS spectra were acquired at 300 K. (B) STM images (298 K, 1.6 V, 0.2 nA) of the initial 700 K annealed surface dominated by Rh_{oct} with few Rh_{met} clusters (top). The same surface was exposed to 2400 Langmuirs of H_2 at 500 K (middle) and subsequently at 700 K (bottom). The schematics illustrate the observed changes in the distribution of the Rh species after each step.

experiments combined provide strong evidence that Rh_{oct} release is induced by the lattice oxygen removal. The reduction of Rh_{oct} coordination due to surface oxygen removal provides a feasible pathway for its release and Rh_{ad} formation. Such dynamically formed Rh_{ad} species are highly active for the formate conversion to CO_2 as demonstrated in Figure 2A. As shown previously, Rh_{ad} can readily cluster at elevated temperatures (>400 K) and form Rh_{met} clusters, as observed by XPS in Figure 4A.[30-31] Though capturing the initial formation of Rh_{ad} in XPS is difficult, prior studies with Pd adatoms supported on $Fe_3O_4(001)$ demonstrate that the Pd will readily mobilize on the surface in a hydroxyl-rich environment.[12] Ultimately, the surface Rh_{ad} and Rh_{met} species readily convert back to Rh_{oct} once the surface intermediates are desorbed and the sample temperature reaches 700 K, as demonstrated in Figure 4A. This behavior aligns with our previous study that showed that small Rh_{metal} clusters < 1.3 nm in diameter are unstable at 700 K and break apart completely, substituting into the $Fe_3O_4(001)$ surface.[31]

2.5 Elucidating destabilization of Rh_{oct} with theory. To further explore the effect of surface hydroxylation and coordination environment reduction on the relative stability of Rh_{oct}, density functional theory (DFT) calculations were performed on a slab model of the reconstructed $Fe_3O_4(001)$ (see SI for computational details and Figure S6).

We first examined the influence of hydroxyl position on the Fe_3O_4 structural rearrangement and the Rh adsorption energy, E_{ads}. Based on the DFT calculations, a mechanism is proposed for converting Rh_{ad} to Rh_{oct}, depicted in Figures 5 & S7. Figure 5A parallels the experimentally observed binding of Rh to the BLO position to form Rh_{ad}. The bidentate Rh_{ad} has an adsorption energy, E_{ads}, of -3.82 eV, Bader charge, BC, of +0.40, and an average Rh-O bond length, $\langle R_{Rh\text{-}O} \rangle$, of 1.98 Å. These results agree with those of Hulva et al., who obtained E_{ads}=-4.50 eV and BC=+0.68 for Rh_{ad}.[7] Hydroxylation (2 OH per unit cell, see Figure 5 caption) increases E_{ads} by 0.70 eV, slightly increases $\langle R_{Rh\text{-}O} \rangle$, and decreases the Rh charge (see Table 1).

The formation of Rh_{oct} is likely initiated by diffusion of an adjacent Fe_{oct} into a subsurface cation vacancy (SCV) (Figure 5B), creating an octahedral Fe vacancy, Fe_{oct}^{vac}, which can be filled by the Rh_{ad} to produce Rh_{oct} (Figure 5D). In this five-fold coordinated environment, Rh_{oct} is significantly more positive (BC = +1.25) and $\langle R_{Rh\text{-}O} \rangle$ increases (Table 1). The Rh_{oct}- small O bond lengths are comparable to Fe_{oct} with $\langle R_{Fe\text{-}O} \rangle$ = 2.00 Å; as such, incorporation of Rh_{oct} necessitates only a limited change to the Fe_3O_4 lattice. The average change in Fe position in the two topmost bilayers upon Rh_{oct} incorporation, relative to reconstructed Fe_3O_4, is only 0.05 Å (0.04 Å for O). This change is largely due to the filling of the SCV; replacing Fe_{oct} with Rh_{oct} without filling the SCV (representing the displaced Fe occupying a bulk defect) results in a change of ~0.02 Å for Fe and O.

From Figure 5C, the Rh_{ad} to Rh_{oct} conversion results in a 0.32 eV slab stabilization. Counter to Rh_{ad}, hydroxylation results in a decrease of $\langle R_{Rh\text{-}O} \rangle$ (Table 1). The comparatively large change is primarily due to the contraction of the axial Rh-O bond (2.24 → 1.98 Å); Rh charge changes negligibly. Hydroxylation consistently stabilizes the slab in all steps from Rh_{ad} to Rh_{oct} by ~0.7 eV, favoring Rh_{oct}. Furthermore, this result is consistent irrespective of which SCV the displaced Fe_{oct}

occupies, including its displacement to the bulk (see Figures S8 & S9 and Tables S1 & S2).

In Figure 5, two hydroxyl groups are present on the O bound to the Fe_{tet}, referred to as OH_{tet}, adjacent to the BLO (the remaining six hydroxyl groups occupy the other 3 BLOs of the cell, OH_{BLO}); this was chosen as OH_{tet} has a similar binding strength to OH_{BLO} (see Figure S10 and Table S3) and for ease of comparison with Rh_{ad} which occupies the BLO site. However, after Rh_{oct} formation, moving the two OH_{tet} to OH_{BLO} results in an additional 0.39 eV slab stabilization (Figure 5C). This negligibly affects Rh_{oct} charge and $<R_{Rh-O}>$ (see Table 1), but does reduce E_{ads} from -7.58 eV (OH_{tet}) to -6.18 eV (OH_{BLO}) due to hydroxyls stabilizing the Rh vacancy formed in the E_{ads} calculation (see the SI for details). Moreover, these OH_{BLO} facilitate the nearby Fe_{int}'s filling of the SCV adjacent to the displaced Fe_{oct}, resulting in a local lifting of the reconstruction (Figure 5E) and a 1.61 eV slab stabilization (relative to Rh_{oct}, Figure 5D). We denote this Rh^{LL}_{oct}. The Fe_{int} vacancy creates a new bulk-like open site, distinguished as BLO'; moving H's from a distant BLO to here results in a further 0.20 eV slab stabilization and a Rh^{LL}_{oct} bound to two OH's (Figures 6A). The local reconstruction lifting significantly stabilizes the Rh^{LL}_{oct} slab relative to Rh_{ad} (2.29 eV).

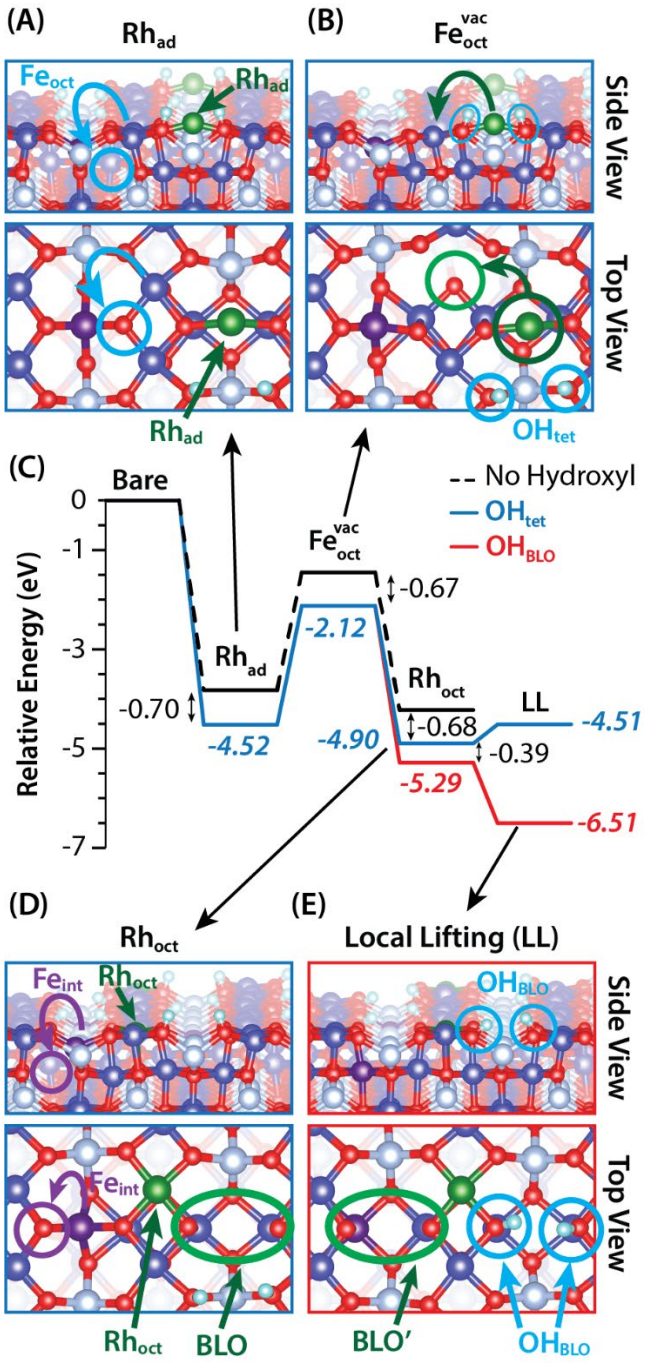

Figure 5. Proposed mechanism for the conversion of Rh_{ad} to Rh_{oct} and the effect of surface hydroxylation. (A,B,D) Structures along $Rh_{ad} \rightarrow Rh_{oct}$ pathway with hydroxyls. (C) Reaction energetics from DFT calculations. (E) Structures depicting the local lifting of the Fe_3O_4 reconstruction. There are 8 hydroxyl on the surface (2 per unit cell)- 6 OH_{BLO} & 2 OH_{tet} (denoted with blue borders) or 8 OH_{BLO} (denoted with red borders). Atom coloring- dark blue: Feoct, blue-grey: Fetet, purple: Feint, red: oxygen, light blue: hydrogen, green: Rh. The Feint atom is colored purple to more easily track the filling of a SCV. See Figure S7 for all structures.

Table 1. DFT calculated Rh adsorption energy, E_{ads}, Bader charge, BC, and average Rh-O bond length, $<R_{Rh-O}>$, on Fe_3O_4(001) surfaces.

Structure	E_{ads} (eV)	Rh BC	$<R_{Rh-O}>$ (Å)
Rh_{ad}	-3.82	+0.40	1.98
Rh_{ad} OH_{tet}[a]	-4.52	+0.32	1.99
Rh_{oct}	-7.80	+1.25	2.07
Rh_{oct} OH_{tet}[a]	-7.58	+1.27	2.04
Rh_{oct} OH_{BLO}	-6.18	+1.25	2.04
Rh^{LL}_{oct}	-7.93	+1.14	2.08
Rh^{LL}_{oct} OH_{tet}[a]	-7.58	+1.33	2.02
Rh^{LL}_{oct} OH_{BLO}	-6.70	+1.03	2.11
Rh^{LL}_{oct} $OH_{BLO+BLO'}$	-5.71	+1.24	2.03
Rh^{LL}_{oct} $OH_{BLO+BLO'}$ $-H_2O$	-5.43	+0.86	2.08
Rh^{LL}_{oct} $OH_{BLO+BLO'}$ $-2H_2O$	-4.94	+0.55	2.08

[a]OH_{tet} structures refer to the hydroxyl configuration of Figures 5A, 5B, & 5D, OH_{BLO} for Figure 5E, and $OH_{BLO+BLO'}$ for Figure 6B.

This result suggests that hydroxylation and the resulting rearrangement preferentially stabilize the Rh_{oct}. As such, it is clear that hydroxylation alone is insufficient to explain the experimentally observed destabilization of Rh_{oct} and conversion to Rh_{ad}. This points to some other process at play during Rh_{oct} destabilization.

Hydroxyl recombination to H_2O through the Mars-van Krevelen mechanism is evidenced by the etch pits of Figure 4. From Figure 2, the loss of H_2O at 500 K coincides with the release of Rh_{oct}, suggesting H_2O formation and loss of lattice O destabilize Rh_{oct}. To investigate this, we performed DFT calculations examining the effect of H_2O loss and oxygen vacancy formation on Rh. The structure of Figure 6A, where the reconstruction is lifted near Rh^{LL}_{oct} and the Rh is adjacent to two hydroxyls, is very favorable (-6.71 eV relative to bare Fe_3O_4). One of these hydroxyls may recombine with the H of an

adjacent OH_{BLO} to produce H_2O and an oxygen vacancy, O_{vac} (Figure 6B-C). The formation of the first O_{vac} decreases both Rh charge and E_{ads} (Table 1). The second O_{vac} formation (Figure 6C-D) produces a tridentate Rh, decreasing the charge and binding to BC = +0.55 and E_{ads} = -4.94 eV. Comparing this to the Rh_{ad} and Rh_{ad}-OH_{tet} surface, we see that water loss causes the Rh_{oct} to become more adatom-like in character and gives similar adsorption energy, supporting the experimental conclusions that oxygen lattice removal via hydroxyl recombination activates Rh_{oct}.

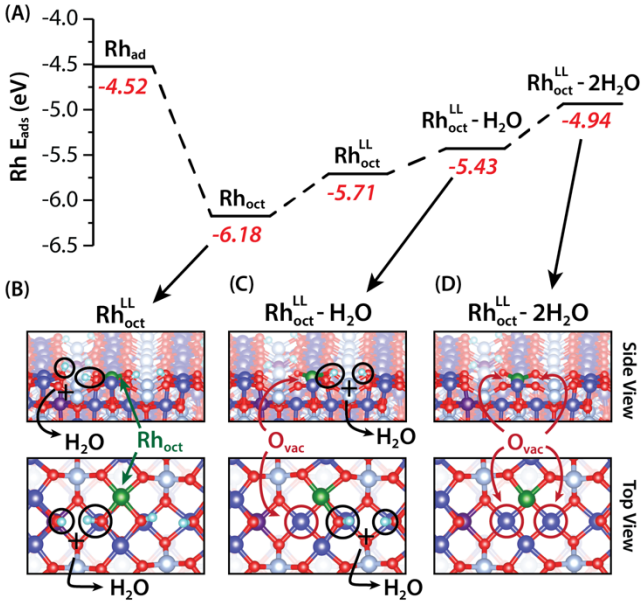

Figure 6. Recombination of hydroxyls at the BLO positions to produce H_2O and oxygen lattice vacancies, O_{vac}, destabilizes Rh_{oct}. Dark blue atoms Fe_{oct}, blue/grey: Fe_{tet}, purple: Fe_{int}, red: oxygen, light blue: hydrogen, green: Rh. The Fe_{int} atom is colored purple to more easily track its filling of a SCV.

3. DISCUSSION

The addition of Rh results in a dramatic shift toward CO_2 production during the decomposition of formic acid vs the clean Fe_3O_4(001) surface. Of these two prepared active sites (adatoms and octahedral), adatoms are the most selective in producing CO_2, with each site having a turnover number as high as 200 formates per Rh single atom. Rh octahedral sites appear to be equally active, desorbing at similar temperatures as the adatom, but require ~17-20 times the Rh coverage as the adatoms to achieve similar desorption products and temperatures hinting at a similar active site. XPS spectra reveal that Rh octahedral converts to Rh adatoms and nanoparticles at reaction temperatures (450-600 K). This may be due to surface hydroxyls forming from the initial deprotonation of formic acid or the reaction of adjacent hydroxyls forming water and an oxygen vacancy. Similar experiments involving the dosing of atomic hydrogen, and hydrogen splitting and spillover from nanoparticles forming surface hydroxyls demonstrate a similar conversion of Rh octahedral to nanoparticles. This conversion is reversible as long as the newly formed Rh nanoparticles are less than 1.3 nm in size, allowing for the regeneration of the Rh octahedral sites after annealing to 700 K. This reversibility is determined by the initial Rh_{oct} coverage, which limits the extent of nanoparticle formation. The conversion of Rh_{oct} to Rh_{met} around formate and hydroxyl reaction temperatures (450-600 K) suggests Rh_{oct} are destabilized by the reaction of adjacent hydroxyls, which form water and oxygen vacancies. The undercoordinated Rh_{oct}, lacking neighboring O-atom(s), is destabilized and converts to a Rh adatom. Rh adatoms are mobile at these reaction temperatures and may sinter into small Rh nanoparticles. This suggests that the Rh adatom and small nanoparticles are the sites responsible for the lower temperature CO_2 activity in the mixed Rh-oxide systems. By identifying the active sites of a model single-atom catalyst, these results have significant implications for understanding the nature of single-atom active sites under reaction conditions.

4. CONCLUSIONS

This study demonstrates how one can activate stable but relatively inactive catalytic sites by adsorbed reactants and intermediates to transiently form metastable but highly active structural motifs. In comparative studies, we show that the catalytic activity of prepared metastable Rh adatoms with separations of tens of nanometers (0.01 Rh_{ad}/u.c.) facilitates efficient conversion of the surface formate species to CO_2 between 480 - 580 K. The annealing (500-700 K) of such metastable catalysts leads to mixed surfaces where Rh is bound in the octahedral Fe sites. The resulting stable Rh_{oct}/Fe_3O_4(001) catalyst structure (also observed on high surface area catalysts) with the same Rh loading is relatively inactive in this redox reaction. At Rh_{oct} loadings of about twenty times higher (~0.2 Rh_{oct}/u.c.), the reaction products and their formation energetics resemble those of Rh_{ad}/Fe_3O_4(001). Detailed analysis proves that surface hydroxyls (prepared from HCOOH, H_2, or H adsorption) are critical for activating stable Rh_{oct} to Rh_{ad} sites. The activation is induced via the water formation reaction step that proceeds via the Mars-van Krevelen mechanism. Surface oxygen removal in this reaction step likely reduces Rh_{oct} coordination, destabilization, and transient formation of a small fraction of Rh_{ad} (~5 %). DFT calculations show that hydroxylation plays a crucial role in stabilizing Rh_{oct}, but the additional process involving OH recombination to H_2O and the formation of O lattice vacancies enables the conversion of the Rh_{oct} to Rh_{ad}. As the surface reaction intermediates are depleted and the sample is heated to 700 K, the transiently formed Rh_{ad} sites are converted back to the stable but inactive Rh_{oct} sites. This study demonstrates the operation of a switchable catalyst that is activated in the presence of surface intermediates and reverts back to a stable but inactive form when the reaction is completed. Dynamic changes in the structure of the active sites observed here further demonstrate how the minority, transiently formed active site can dominate the reactivity and lead to challenges in identifying the active sites on more complex high-surface-area materials. Since the lattice oxygen participation via the Mars-van Krevelen mechanism is common in many acid-base and redox catalytic reactions, this single-atom catalyst activation can broadly apply to many systems.

ASSOCIATED CONTENT

Data Availability Statement

All data in the study are available from the corresponding authors upon reasonable request.

Supporting Information

Supporting Information is available free of charge at http://pubs.acs.org.

List of content: Materials and methods, Rh 3d XPS of 0.05 Rh/u.c., Formic acid TPRS on 1.0 Rh/u.c., XPS Fe 2p with formic acid and atomic deuterium, Repeat TPRS on 1.0 Rh/u.c. and 0.17 Rh/u.c., image of DFT slab model used, full DFT calculated mechanism of adatom to octahedral conversion, DFT calculations of hydroxylated Rh octahedral surfaces, adsorption energy diagram of different Rh surfaces, tables of relative energies along adatom to octahedral conversion, slabs of different hydroxyl positions tested, and table of energies for different hydroxyl positions.

AUTHOR INFORMATION

Corresponding Authors

*Zdenek Dohnálek
Email: zdenek.dohnalek@pnnl.gov
*Mal-Soon Lee
Email: malsoon.lee@pnnl.gov

Author Contributions

† These authors contributed equally.

The manuscript was written through contributions of all authors.

Conflict of Interest Disclosure

Authors declare that they have no competing interests.

Preprint servers

ChemRxiv: https://doi.org/10.26434/chemrxiv-2024-dpck2

Funding Sources

U.S. Department of Energy, Office of Science, Basic Energy Sciences, Chemical Sciences, Geosciences, and Biosciences Division, Catalysis Science Program, FWP 47319.

Acknowledgment

This work was supported by the U.S. Department of Energy, Office of Science, Basic Energy Sciences, Chemical Sciences, Geosciences, and Biosciences Division, Catalysis Science Program, FWP 47319. PNNL is a multiprogram national laboratory operated for DOE by Battelle under Contract DE-AC05-76RL01830. Computational resources were provided by a user proposal at the National Energy Research Scientific Computing Center located at Lawrence Berkley National Laboratory.

References

(1) Wang, A.; Li, J.; Zhang, T. Heterogeneous single-atom catalysis. Nat. Rev. Chem. **2018**, 2 (6), 65-81. DOI: 10.1038/s41570-018-0010-1

(2) Mitchell, S.; Perez-Ramirez, J. Single atom catalysis: a decade of stunning progress and the promise for a bright future. Nat. Commun. **2020**, 11 (1), 4302. DOI: 10.1038/s41467-020-18182-5

(3) Parkinson, G. S. Atomic scale insights into single-atom catalysis. Vak. Forsch. Prax. **2018**, 30 (5), 45-49. DOI: 10.1002/vipr.201800695

(4) Resasco, J.; DeRita, L.; Dai, S.; Chada, J. P.; Xu, M.; Yan, X.; Finzel, J.; Hanukovich, S.; Hoffman, A. S.; Graham, G. W.; Bare, S. R.; Pan, X. Christopher, P., Uniformity is key in defining structure-function relationships for atomically dispersed metal catalysts: The case of Pt/CeO_2. J. Am. Chem. Soc. **2020**, 142 (1), 169-184. DOI: 10.1021/jacs.9b09156

(5) Matsubu, J. C.; Yang, V. N.; Christopher, P. Isolated metal active site concentration and stability control catalytic CO_2 reduction selectivity. J. Am. Chem. Soc. **2015**, 137 (8), 3076-84. DOI: 10.1021/ja5128133

(6) Parkinson, G. S.; Novotny, Z.; Argentero, G.; Schmid, M.; Pavelec, J.; Kosak, R.; Blaha, P.; Diebold, U. Carbon monoxide-induced adatom sintering in a $Pd–Fe_3O_4$ model catalyst. Nat. Mater. **2013**, 12 (8), 724-728. DOI: 10.1038/nmat3667

(7) Hulva, J.; Meier, M.; Bliem, R.; Jakub, Z.; Kraushofer, F.; Schmid, M.; Diebold, U.; Franchini, C.; Parkinson, G. S. Unraveling CO adsorption on model single-atom catalysts. Science **2021**, 371 (6527), 375-379. DOI: 10.1126/science.abe5757

(8) Zhu, Y.; Yuk, S. F.; Zheng, J.; Nguyen, M. T.; Lee, M. S.; Szanyi, J.; Kovarik, L.; Zhu, Z.; Balasubramanian, M.; Glezakou, V. A.; Fulton, J. L.; Lercher, J. A.; Rousseau, R.; Gutierrez, O. Y. Environment of metal-O-Fe bonds enabling high activity in CO_2 reduction on single metal atoms and on supported nanoparticles. J. Am. Chem. Soc. **2021**, 143 (14), 5540-5549. DOI: 10.1021/jacs.1c02276

(9) Chen, L.; Unocic, R. R.; Hoffman, A. S.; Hong, J.; Braga, A. H.; Bao, Z.; Bare, S. R.; Szanyi, J. Unlocking the catalytic potential of TiO_2-supported Pt single atoms for the reverse water-gas shift reaction by altering their chemical environment. J. Am. Chem. Soc. Au **2021**, 1 (7), 977-986. DOI: 10.1021/jacsau.1c00111

(10) Kraushofer, F.; Parkinson, G. S. Single-atom catalysis: Insights from model systems. Chem. Rev. **2022**, 122 (18), 14911-14939. DOI: 10.1021/acs.chemrev.2c00259

(11) Yang, X. F.; Wang, A.; Qiao, B.; Li, J.; Liu, J.; Zhang, T. Single-atom catalysts: a new frontier in heterogeneous catalysis. Acc. Chem. Res. **2013**, 46 (8), 1740-8. DOI: 10.1021/ar300361m

(12) Doudin, N.; Yuk, S. F.; Marcinkowski, M. D.; Nguyen, M.-T.; Liu, J.-C.; Wang, Y.; Novotny, Z.; Kay, B. D.; Li, J.; Glezakou, V. A.; Parkinson, G.; Rousseau, R.; Dohnálek, Z. Understanding heterolytic H2 cleavage and water-assisted hydrogen spillover on Fe_3O_4(001)-supported single palladium atoms. ACS Catal. **2019**, 9 (9), 7876-7887. DOI: 10.1021/acscatal.9b01425

(13) Liu, J. Catalysis by supported single metal atoms. ACS Catal. **2016**, 7 (1), 34-59. DOI: 10.1021/acscatal.6b01534

(14) Liu, L.; Corma, A. Metal catalysts for heterogeneous catalysis: From single atoms to nanoclusters and nanoparticles. Chem. Rev. **2018**, 118 (10), 4981-5079. DOI: 10.1021/acs.chemrev.7b00776

(15) Kaiser, S. K.; Chen, Z.; Faust Akl, D.; Mitchell, S.; Perez-Ramirez, J. Single-atom catalysts across the periodic table. Chem. Rev. **2020**, 120 (21), 11703-11809. DOI: 10.1021/acs.chemrev.0c00576

(16) Wei, H.; Liu, X.; Wang, A.; Zhang, L.; Qiao, B.; Yang, X.; Huang, Y.; Miao, S.; Liu, J.; Zhang, T. FeO_x-supported platinum single-atom and pseudo-single-atom catalysts for chemoselective hydrogenation of functionalized nitroarenes. Nat. Commun. **2014**, 5, 5634. DOI: 10.1038/ncomms6634

(17) Hannagan, R. T.; Giannakakis, G.; Flytzani-Stephanopoulos, M.; Sykes, E. C. H. Single-atom alloy catalysis. Chem. Rev. **2020**, 120 (21), 12044-12088. DOI: 10.1021/acs.chemrev.0c00078

(18) Mitchell, S.; Vorobyeva, E.; Perez-Ramirez, J. The multifaceted reactivity of single-atom heterogeneous catalysts. Angew. Chem., Int. Ed. Engl. **2018**, 57 (47), 15316-15329. DOI: 10.1002/anie.201806936

(19) Daelman, N.; Capdevila-Cortada, M.; Lopez, N. Dynamic charge and oxidation state of Pt/CeO_2 single-atom catalysts. Nat. Mater. **2019**, 18 (11), 1215-1221. DOI: 10.1038/s41563-019-0444-y

(20) Ren, Y.; Tang, Y.; Zhang, L.; Liu, X.; Li, L.; Miao, S.; Sheng Su, D.; Wang, A.; Li, J.; Zhang, T. Unraveling the coordination structure-

performance relationship in Pt_1/Fe_2O_3 single-atom catalyst. Nat. Commun. **2019**, 10 (1), 4500. DOI: 10.1038/s41467-019-12459-0

(21) Wang, L.; Zhang, W.; Wang, S.; Gao, Z.; Luo, Z.; Wang, X.; Zeng, R.; Li, A.; Li, H.; Wang, M.; Zheng, X.; Zhu, J.; Zhang, W.; Ma, C.; Si, R.; Zeng, J. Atomic-level insights in optimizing reaction paths for hydroformylation reaction over Rh/CoO single-atom catalyst. Nat. Commun. **2016**, 7, 14036. DOI: 10.1038/ncomms14036

(22) Liu, W.; Zhang, L.; Liu, X.; Liu, X.; Yang, X.; Miao, S.; Wang, W.; Wang, A.; Zhang, T. Discriminating catalytically active FeNx species of atomically dispersed Fe-N-C catalyst for delective oxidation of the C-H Bond. J. Am. Chem. Soc. **2017**, 139 (31), 10790-10798. DOI: 10.1021/jacs.7b05130

(23) Mitchell, S.; Pérez-Ramírez, J. Atomically precise control in the design of low-nuclearity supported metal catalysts. Nat. Rev. Mater. **2021**, 6 (11), 969-985. DOI: 10.1038/s41578-021-00360-6

(24) Parkinson, G. S. Unravelling single atom catalysis: The surface science approach. Chinese J. Catal. **2017**, 38 (9), 1454-1459. DOI: 10.1016/s1872-2067(17)62878-x

(25) Bliem, R.; McDermott, E.; Ferstl, P.; Setvin, M.; Gamba, O.; Pavelec, J.; Schneider, M. A.; Schmid, M.; Diebold, U.; Blaha, P.; Hammer, L.; Parkinson, G. S. Subsurface cation vacancy stabilization of the magnetite (001) surface. Science **2014**, 346 (6214), 1215-1218. DOI: 10.1126/science.1260556

(26) Novotny, Z.; Argentero, G.; Wang, Z.; Schmid, M.; Diebold, U.; Parkinson, G. S. Ordered array of single adatoms with remarkable thermal stability: $Au/Fe_3O_4(001)$. Phys. Rev. Lett. **2012**, 108 (21), 216103. DOI: 10.1103/PhysRevLett.108.216103

(27) Bliem, R.; van der Hoeven, J. E.; Hulva, J.; Pavelec, J.; Gamba, O.; de Jongh, P. E.; Schmid, M.; Blaha, P.; Diebold, U.; Parkinson, G. S. Dual role of CO in the stability of subnano Pt clusters at the $Fe_3O_4(001)$ surface. Proc. Natl. Acad. Sci. U.S.A. **2016**, 113 (32), 8921-8926. DOI: 10.1073/pnas.1605649113

(28) Bliem, R.; Kosak, R.; Perneczky, L.; Novotny, Z.; Gamba, O.; Fobes, D.; Mao, Z.; Schmid, M.; Blaha, P.; Diebold, U.; Parkinson, G. S. Cluster nucleation and growth from a highly supersaturated adatom phase: Silver on magnetite. ACS Nano **2014**, 8 (7), 7531-7. DOI: 10.1021/nn502895s

(29) Jakub, Z.; Hulva, J.; Meier, M.; Bliem, R.; Kraushofer, F.; Setvin, M.; Schmid, M.; Diebold, U.; Franchini, C.; Parkinson, G. S. Local structure and coordination define adsorption in a model Ir_1/Fe_3O_4 single-atom catalyst. Angew. Chem. Int. Ed. **2019**, 58 (39), 13961-13968. DOI: 10.1002/anie.201907536

(30) Jakub, Z.; Hulva, J.; Ryan, P. T. P.; Duncan, D. A.; Payne, D. J.; Bliem, R.; Ulreich, M.; Hofegger, P.; Kraushofer, F.; Meier, M.; Schmid, M.; Diebold, U.; Parkinson, G. S. Adsorbate-induced structural evolution changes the mechanism of CO oxidation on a $Rh/Fe_3O_4(001)$ model catalyst. Nanoscale **2020**, 12 (10), 5866-5875. DOI: 10.1039/c9nr10087c

(31) Sharp, M. A.; Lee, C. J.; Mahapatra, M.; Smith, R. S.; Kay, B. D.; Dohnálek, Z. Preparation and characterization of model homotopic catalysts: Rh adatoms, nanoparticles, and mixed oxide surfaces on $Fe_3O_4(001)$. J. Phys. Chem. C **2022**, 126 (34), 14448-14459. DOI: 10.1021/acs.jpcc.2c03426

(32) Gawish, M. A.; Drmosh, Q. A.; Onaizi, S. A. Single atom catalysts: An overview of the coordination and interactions with metallic supports. Chem. Rec. **2022**, 22 (7), e202100328. DOI: 10.1002/tcr.202100328

(33) Qi, K.; Chhowalla, M.; Voiry, D. Single atom is not alone: Metal–support interactions in single-atom catalysis. Mater. Today **2020**, 40, 173-192. DOI: 10.1016/j.mattod.2020.07.002

(34) Kraushofer, F.; Resch, N.; Eder, M.; Rafsanjani-Abbasi, A.; Tobisch, S.; Jakub, Z.; Franceschi, G.; Riva, M.; Meier, M.; Schmid, M.; Diebold, U.; Parkinson, G. S. Surface reduction state determines stabilization and incorporation of Rh on α-$Fe_2O_3(11\bar{0}2)$. Adv. Mater. Interfaces **2021**, 8 (8), 2001908. DOI: 10.1002/admi.202001908

(35) Wang, X.; Shi, H.; Kwak, J. H.; Szanyi, J. Mechanism of CO_2 hydrogenation on Pd/Al_2O_3 catalysts: Kinetics and transient DRIFTS-MS studies. ACS Catal. **2015**, 5 (11), 6337-6349. DOI: 10.1021/acscatal.5b01464

(36) Ratnasamy, C.; Wagner, J. P. Water gas shift catalysis. Catal. Rev. - Sci. Eng. **2009**, 51 (3), 325-440. DOI: 10.1080/01614940903048661

(37) Senanayake, S. D.; Stacchiola, D.; Evans, J.; Estrella, M.; Barrio, L.; Pérez, M.; Hrbek, J.; Rodriguez, J. A. Probing the reaction intermediates for the water–gas shift over inverse $CeO_x/Au(111)$ catalysts. J. Catal. **2010**, 271 (2), 392-400. DOI: 10.1016/j.jcat.2010.02.024

(38) Barteau, M. A. Site requirements of reactions on oxide surfaces. J. Vac. Sci. Technol., A **1993**, 11 (4), 2162-2168. DOI: 10.1116/1.578386

(39) Vohs, J. M. Site requirements for the adsorption and reaction of oxygenates on metal oxide surfaces. Chem. Rev. **2013**, 113 (6), 4136-63. DOI: 10.1021/cr300328u

(40) Vohs, J. M.; Barteau, M. A. Conversion of methanol, formaldehyde and formic acid on the polar faces of zinc oxide. Surf. Sci. **1986**, 176 (1-2), 91-114. DOI: 10.1016/0039-6028(86)90165-2

(41) Peng, X. D.; Barteau, M. A. Dehydration of carboxylic acids on the MgO(100) surface. Catal. Lett. **1991**, 7 (5-6), 395-402. DOI: 10.1007/bf00764930

(42) Vohs, J. M.; Barteau, M. A. Reaction pathways and intermediates in the decomposition of acetic and propionic acids on the polar surfaces of zinc oxide. Surf. Sci. **1988**, 201 (3), 481-502. DOI: 10.1016/0039-6028(88)90499-2

(43) Henderson, M. A. Complexity in the decomposition of formic acid on the $TiO_2(110)$ surface. J. Phys. Chem. B **1997**, 101 (2), 221-229. DOI: 10.1021/jp961494i

(44) Stubenrauch, J.; Brosha, E.; Vohs, J. M. Reaction of carboxylic acids on $CeO_2(111)$ and $CeO_2(100)$. Catal. Today **1996**, 28 (4), 431-441. DOI: 10.1016/s0920-5861(96)00251-9

(45) Senanayake, S. D.; Mullins, D. R. Redox pathways for HCOOH decomposition over CeO_2 surfaces. J. Phys. Chem. C **2008**, 112 (26), 9744-9752. DOI: 10.1021/jp8016425

(46) Gamba, O.; Noei, H.; Pavelec, J.; Bliem, R.; Schmid, M.; Diebold, U.; Stierle, A.; Parkinson, G. S. Adsorption of formic acid on the $Fe_3O_4(001)$ surface. J. Phys. Chem. C **2015**, 119 (35), 20459-20465. DOI: 10.1021/acs.jpcc.5b05560

(47) Bliem, R.; van der Hoeven, J.; Zavodny, A.; Gamba, O.; Pavelec, J.; de Jongh, P. E.; Schmid, M.; Diebold, U.; Parkinson, G. S. An atomic-scale view of CO and H_2 oxidation on a Pt/Fe_3O_4 model catalyst. Angew. Chem. Int. Ed. **2015**, 54 (47), 13999-14002. DOI: 10.1002/anie.201507368

(48) Parkinson, G. S.; Mulakaluri, N.; Losovyj, Y.; Jacobson, P.; Pentcheva, R.; Diebold, U. Semiconductor–half metal transition at the $Fe_3O_4(001)$ surface upon hydrogen adsorption. Phys. Rev. B **2010**, 82 (12), 125413. DOI: 10.1103/PhysRevB.82.125413

For Table of Contents Only